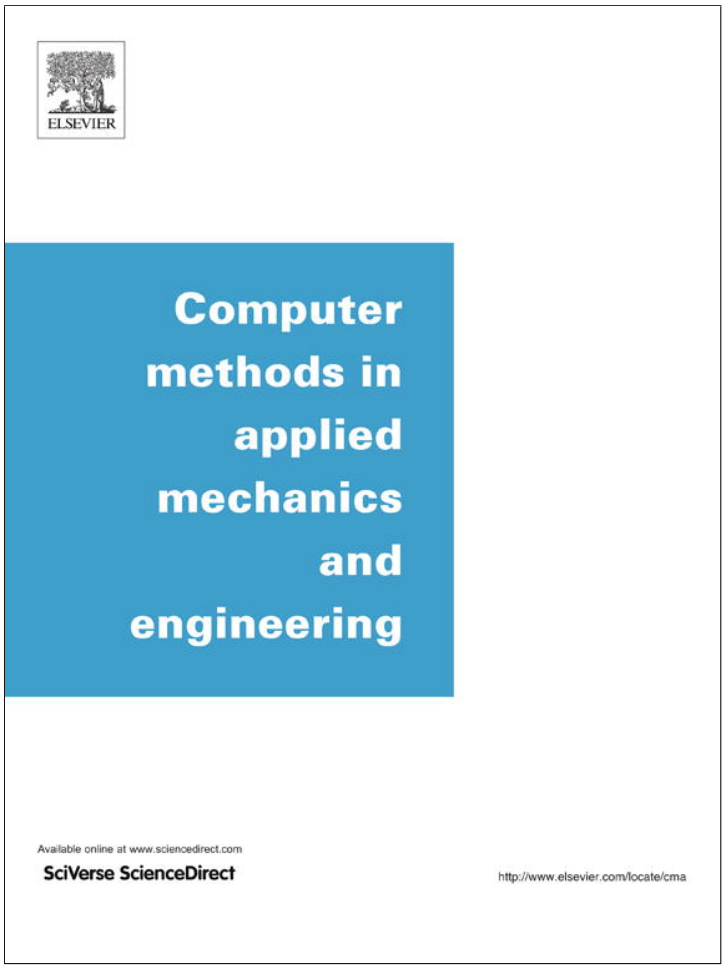

(This is a sample cover image for this issue. The actual cover is not yet available at this time.)

Comput. Methods Appl. Mech. Engrg. 241–244 (2012) 275–285

Contents lists available at SciVerse ScienceDirect

Comput. Methods Appl. Mech. Engrg.

journal homepage: www.elsevier.com/locate/cma

An adaptive finite element material point method and its application in extreme deformation problems ☆

Y.P. Lian, X. Zhang *, Y. Liu

AML, School of Aerospace, Tsinghua University, Beijing 100084, PR China

ARTICLE INFO

Article history:
Received 7 March 2012
Received in revised form 24 May 2012
Accepted 20 June 2012
Available online 28 June 2012

Keywords:
Material point method
Adaptive finite element method
Impact
Penetration
Soil collapse

ABSTRACT

Taking advantages of both Lagrangian and Eulerian methods, material point method (MPM) is suitable for modeling problems with extreme deformation. However, MPM is less accurate and less efficient than finite element method (FEM) for small deformation problems due to particle quadrature and mappings between particles and background grid applied in MPM. To take advantages of both FEM and MPM, an adaptive finite element material point method is developed for modeling the dynamic behavior of material under extreme loading. Bodies are initially discretized by finite elements, and then the elements with large strain are adaptively converted into MPM particles based on their degree of distortion or plastic strain during the solution process. The interaction between the remaining finite elements and MPM particles is implemented based on the background grid in MPM framework. Several numerical examples are presented to validate the efficiency and accuracy of the proposed method, and the numerical results are in good agreement with experiments, while the efficiency of the method is higher than that of both MPM and FEM.

1. Introduction

Numerical simulation of extreme deformation problems such as explosion, impact and landslide problems is a very active research topic. The Lagrangian finite element method (FEM) has been developed maturely and used in various numerical analyzes, but suffers from mesh tangling which may deteriorate its numerical accuracy and efficiency dramatically for all such problems. Recently, a lot of effort has been devoted to develop new high-performance finite element models which are less sensitive to mesh tangling, such as quadrilateral membrane element by the quadrilateral area coordinate method [1], 4-node hybrid stress-function membrane element by the principle of minimum complementary energy [2], etc. In contrast to Lagrangian method, Eulerian methods use Eulerian mesh without element distortion, but encounter difficulties in capturing the material interfaces and tracking the internal history variables. In addition, the arbitrary Lagrangian Eulerian method [3] was developed to take advantages of both FEM and Eulerian methods, which has been applied in 2D problems successfully. However, developing an effective and efficient mesh moving scheme for complicated 3D problems is still a big challenge. Furthermore, the convective effects due to the mass flux between adjacent cells in Eulerian framework could still cause dissipation and dispersion problems.

Since the 90s of the last century, many researches have been focusing on the meshless/particle methods to expand the capacity of numerical methods for all such problems within the Lagrangian framework. The basic idea for these methods is to discretize the material domain by a set of particles instead of mesh and construct the trial functions based on the particles. Hence, all such methods without the mesh dependence are suitable for problems with extreme deformation. Until now, many meshless methods have been proposed with successful applications, such as the smoothed particle hydrodynamics (SPH) method [4,5], the element free Galerkin (EFG) method [6,7], the reproducing kernel particle (RKPM) method [8,9], just to name a few. But the efficiency of all such methods is lower than that of FEM for small deformation problems and they suffer from their inherent shortcomings [10]. For higher accuracy, the trial functions used in meshless methods are often complicated which make the essential boundary conditions complicated to apply compared with FEM. Hence, much effort has been devoted to couple these methods with FEM to benefit from the advantages of both methods and avoid their shortcomings [11–14]. The coupling algorithms include master–slave coupling, coupling via mixed interpolation, coupling via Lagrange multipliers, coupling via a bridge domain, etc. Among them, Johnson et al. proposed an algorithm to automatically convert distorted finite elements into meshless particles for 2D and 3D [15,16]. Such coupling works are reviewed by Rabczuk et al. in detail in [17]. In

☆ Supported by National Basic Research Program of China (2010CB832701).
* Corresponding author.
E-mail address: xzhang@tsinghua.edu.cn (X. Zhang).

0045-7825/$ - see front matter © 2012 Elsevier B.V. All rights reserved.
http://dx.doi.org/10.1016/j.cma.2012.06.015

addition to coupling methods, Fahrenthold and Horban [18] developed a hybrid particle–element method, which uses both elements and particles for whole material region without element-to-particle converting.

Among meshless methods, material point method (MPM) [19] takes the advantages of both Lagrangian and Eulerian methods. In MPM, the material domain is discretized by a set of Lagrangian particles which carry all the state variables, such as position, velocity, stress, strain, etc. An Eulerian background grid covering all the material domain is used to integrate the momentum equations and calculate the spacial derivatives. Unlike others meshless methods, the trial functions used in MPM are the same to that of FEM. So MPM shows some advantages over other meshless methods in efficiency and tension stability [20]. Furthermore, it is easy to impose the essential boundary conditions and a no-slip contact constraint is inherent in MPM due to the single-valued velocity field used to update all the particles.

By now, significant effort has been devoted to the development of MPM. Bardenhagen and Kober [21] developed a generalized interpolation material point (GIMP) method to suppress the artificial noise when the particles moving across the cell, due to the discontinuity of the gradient of the standard shape function used in the original MPM. Ma et al. [22] proposed an adaptive particle splitting scheme for MPM to avoid the numerical fracture when two particles are separated by a grid cell. Based on the Lagrangian multiplier method, much work has been done to build the contact/friction/separation algorithm of MPM [23–25], where the impenetrability condition and Coulomb friction model are carried out on the background grid. Ma et al. [26] proposed an accurate contact detection method to avoid contact occurring earlier than the actual time and also developed a local multi-grid contact method based on the work of Hu and Chen [27]. MPM and its extensions have been used for many problems involving extreme deformation, such as explosion and impact [28,29], geomechanics [30,31], cracking expansion [32], multiphase flows [33], just to name a few. However, the efficiency of MPM is lower than that of FEM due to the mappings between background grid and particles, while the accuracy of particles quadrature used in MPM is lower than that of Gauss quadrature used in FEM. Hence, Zhang et al. [34] developed an explicit material point finite element method (MPFEM) to combine the advantages of both FEM and MPM. In MPFEM, the material domain is discretized by finite elements with a predefined background grid in the anticipated large deformation region. The finite element nodes covered by the background grid are converted into MPM particles automatically during the simulation process. But, users are required to identify the potential large deformation region to place the background grid. Furthermore, elements with mild deformation are converted into particles once they move into the predefined background grid. Recently, Lian et al. [35] proposed a coupled finite element material point (CFEMP) method, in which the body with mild deformation is discretized by finite elements, while the body with extreme deformation is discretized by MPM particles. The interaction between them is implemented by contact method carried out on the background grid. However, users are also required to identify the body which will experience extreme deformation.

To take full advantages of both FEM and MPM, an adaptive finite element material point (AFEMP) method is proposed in this paper. In AFEMP method, bodies are initially discretized by finite elements, and then the distorted elements are adaptively converted into MPM particles when their plastic strain or distortion degree exceed a user prescribed value during the simulation process. The interaction between the remaining finite elements and MPM particles is implemented based on the background grid in MPM framework. Hence, the material region with mild deformation is modeled by finite elements, while the material region with extreme deformation is modeled by MPM particles automatically.

In this paper, AFEMP method is first validated by two problems of two-rod impact and Taylor bar impact, and then applied to study the penetration of a WHA long rod projectile to a steel plate and the soil collapse problems. The numerical results are in good agreement with the analytical results and experimental data, while the efficiency of AFEMP is higher than that of both FEM and MPM especially for problems involving extreme deformation.

The remaining part of this paper is organized as follows. Section 2 gives the detail of the discretization of momentum equations by AFEMP method. The element–particle conversion algorithm is proposed in Section 3 and the coupling algorithm between the remaining finite elements and the converted particles is presented in Section 4. The description of the numerical implementation is presented in Section 5, while the numerical examples are listed in Section 6. Finally, the conclusions are summarized in Section 7.

2. AFEMP method

2.1. Discretization scheme

In AFEMP method, a material region Ω shown in Fig. 1(a) is initially discretized into finite elements as shown in Fig. 1(b). During the simulation process, the distorted element is automatically converted into MPM particles as shown in Fig. 1(c) where regular Eulerian background grid is used to cover all the MPM particles. Therefore, the material region is discretized by both mesh and particles together, but the trial functions are constructed via the mesh including finite element mesh and background grid.

2.2. Governing equations

In the updated Lagrangian framework, the governing equations for the material domain Ω shown in Fig. 1(a) are given as

$$\rho(\boldsymbol{X},t)J(\boldsymbol{X},t)=\rho_0(\boldsymbol{X}) \tag{1}$$

$$\nabla\cdot\boldsymbol{\sigma}+\rho\boldsymbol{b}=\rho\ddot{\boldsymbol{u}} \tag{2}$$

$$\begin{cases}(n_j\sigma_{ij})|_{\Gamma_t}=\bar{t}_i\\ u_i|_{\Gamma_u}=\bar{u}_i\end{cases} \tag{3}$$

$$\begin{cases}\dot{\boldsymbol{u}}(\boldsymbol{X},0)=\dot{\boldsymbol{u}}_0(\boldsymbol{X})\\ \boldsymbol{u}(\boldsymbol{X},0)=\boldsymbol{u}(\boldsymbol{X})\end{cases} \tag{4}$$

where ρ is the current density, J is the Jacobian and $\boldsymbol{X}$ is the Lagrangian coordinate. Subscript 0 signifies the initial value, t is the current time, $\boldsymbol{\sigma}$ is the Cauchy stress, $\boldsymbol{b}$ is the body force per unit mass, the superimposed dot indicates the time derivatives, $\boldsymbol{u}$ is the displacement, subscripts i and j denote the components of the space with Einstein summation convention, and n_j is the unit outward normal to the boundary. Γ_t and Γ_u signify the prescribed traction boundary and displacement boundary of Ω, respectively. Taking the virtual displacement δu_i as the test function, the weak form of Eq. (2) can be obtained as

$$\int_\Omega\rho\ddot{u}_i\delta u_i d\Omega+\int_\Omega\sigma_{ij}\delta u_{i,j}d\Omega-\int_\Omega\rho b_i\delta u_i d\Omega-\int_{\Gamma_t}\bar{t}_i\delta u_i d\Gamma=0 \tag{5}$$

This weak form will be solved by FEM and MPM solution schemes in AFEMP method.

2.3. Solution scheme

AFEMP method includes FEM and MPM solution schemes, which are similar. In AFEMP, distorted elements are automatically converted into MPM particles during the simulation process. Therefore, the material domain may consist of both finite elements

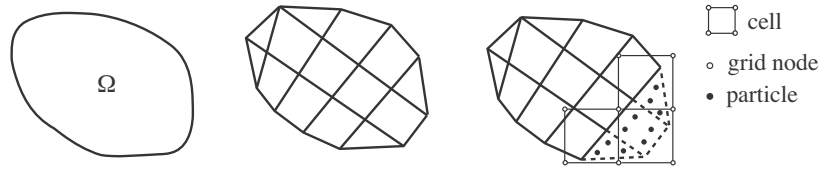

Fig. 1. A material domain with AFEMP discretization.

and MPM particles with a background grid, as shown in Fig. 1(c). In each time step, the particles are attached rigidly to the background grid and deform with it. Hence the solution scheme for MPM particles is similar to that of FEM with taking the particles as quadrature points.

In both FEM and MPM, the displacement u is approximated as

$$u_i = \sum_{I=1}^{n} N_I u_{iI} \tag{6}$$

where the subscript I denotes the FE node in FEM domain and the background grid node in MPM domain, respectively. N_I is the corresponding shape function, n is the total number of nodes in an element in FEM domain or grid nodes in a background cell in MPM domain, and u_{iI} is the displacement of node I in i direction. The same type of elements are used in both FEM domain and MPM background grid. Taking the eight-node hexahedral element as an example, the shape functions are given by

$$N_I = \frac{1}{8}(1+\xi\xi_I)(1+\eta\eta_I)(1+\zeta\zeta_I), \quad I = 1,2,\ldots,8 \tag{7}$$

where (ξ_I, η_I, ζ_I) are the nature coordinates of element node I in the parent domain ($\xi \in [-1,1]$, $\eta \in [-1,1]$, $\zeta \in [-1,1]$).

Substituting Eq. (6) into Eq. (5) yields

$$\dot{p}_{iI} = f_{iI}^{\text{int}} + f_{iI}^{\text{ext}} \tag{8}$$

where

$$p_{iI} = m_I v_{iI} \tag{9}$$

is the nodal momentum, m_I is the nodal mass, v_{iI} is the nodal velocity,

$$f_{iI}^{\text{int}} = -\sum_e \int_{V_e} N_{I,j}\sigma_{ji} dV \tag{10}$$

is the internal nodal force, and

$$f_{iI}^{\text{ext}} = \sum_e \left(\int_{V_e} \rho N_I b_i dV + \int_{\Gamma_{te}} N_I \bar{t}_i d\Gamma \right) \tag{11}$$

is the external nodal force. In AFEMP, the lumped mass matrix is used for both elements and particles. For FEM, volume integration is carried out with one-point integration, so that Eqs. (10) and (11) can be rewritten, respectively, as

$$f_{iI}^{\text{int}} = -\sum_e N_{eI,j}\sigma_{jie} V_e \tag{12}$$

$$f_{iI}^{\text{ext}} = \sum_e \left(M_e N_{eI} b_{ei} + \int_{\Gamma_{te}} N_I \bar{t}_i d\Gamma \right) \tag{13}$$

where e denotes element, $M_e = \rho_e V_e$. Moreover, the hourglass-resisting force must be added to the right side of Eq. (11) to control the hourglass modes. Thus the total nodal force is composed of three parts, namely

$$f_{iI} = f_{iI}^{\text{ext}} + f_{iI}^{\text{int}} + f_{iI}^{\Gamma} \tag{14}$$

For MPM, mass and momentum of particles are mapped to the background grid at the beginning of each time step via the shape functions, namely

$$m_I = \sum_{p=1}^{n_p} N_{Ip} m_p \tag{15}$$

$$p_{iI} = \sum_{p=1}^{n_p} N_{Ip} m_p v_{ip} \tag{16}$$

where the subscript p denotes the MPM particle, n_p is the total number of MPM particles. The volume integration in MPM is carried out with particles integration, so that the Eqs. (10) and (11) can be rewritten, respectively, as

$$f_{iI}^{\text{int}} = -\sum_{p=1}^{n_p} N_{Ip,j}\sigma_{ijp}\frac{m_p}{\rho_p} \tag{17}$$

$$f_{iI}^{\text{ext}} = \sum_{p=1}^{n_p} N_{Ip}\bar{t}_{ip}h^{-1}\frac{m_p}{\rho_p} + \sum_{p=1}^{n_p} m_p N_{Ip} b_{ip} \tag{18}$$

Thus the background grid nodal force is given by

$$f_{iI} = f_{iI}^{\text{ext}} + f_{iI}^{\text{int}} \tag{19}$$

In AFEMP method, the central difference method with variable time step size is used to integrate the momentum equation Eq. (8). As shown in Fig. 2, $t^{k+1} = t^k + \Delta t^{k+1/2}$, $t^{k+1/2} = t^k + \Delta t^{k+1/2}/2 = t^{k-1/2} + \Delta t^k$ and $\Delta t^k = (\Delta t^{k-1/2} + \Delta t^{k+1/2})/2$, where k denotes the kth time step.

The critical time step size is determined by

$$\Delta t = \min(L_e/c) \tag{20}$$

where L_e is the characteristic length of element e in FEM domain and the cell e in MPM domain, c is the material sound speed. If a regular background grid used in MPM, L_e is the cell size.

Therefore, the nodal velocities of FE node I are updated by

$$v_{iI}^{k+1/2} = v_{iI}^{k-1/2} + (f_{iI}^{k,\text{int}} + f_{iI}^{k,\text{ext}} + f_{iI}^{\Gamma})\Delta t^k / M_n \tag{21}$$

and the nodal positions at time t^{k+1} are updated by

$$x_{iI}^{k+1} = x_{iI}^{k} + v_{iI}^{k+1/2}\Delta t^{k+1/2} \tag{22}$$

For MPM particle p, its velocities and positions are updated by the nodal velocities and accelerations of background grid nodes, respectively, as

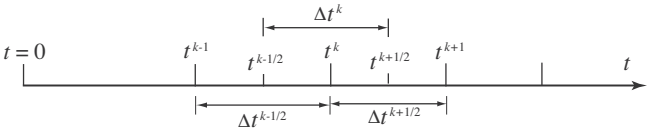

Fig. 2. Time integration.

$$v_{ip}^{k+1/2} = v_{ip}^{k-1/2} + \sum_{I=1}^{n_g} f_{iI}^k N_{pI}^k / m_I^k \Delta t^k \tag{23}$$

$$x_{ip}^{k+1} = x_{ip}^k + \Delta t^{k+1/2} \sum_{I=1}^{n_g} p_{iI}^{k+1/2} N_{pI}^k / m_I^k \tag{24}$$

where $p_{iI}^{k+1/2} = p_{iI}^{k-1/2} + f_{iI}^k \Delta t^k$. At the end of the time step, the deformed background grid is discarded and a new regular background grid is used in the next time step, while the finite element mesh is embedded with the material domain.

Based on the aforementioned discussion, we can find that there are two fundamental differences between FEM and MPM. Firstly, the Gauss points are taken as quadrature points in FEM, while the particles are taken as quadrature points in MPM. Secondly, the mesh is embedded in and deforms with the material domain during the solution process in FEM, whereas the grid is only temporarily embedded in and deform with the material domain in the current time step in MPM. Therefore, it is straightforward to convert the elements with large strain into MPM particles by replacing the Gauss quadrature with particle quadrature and the finite element mesh with the background grid.

3. Conversion algorithm

In this section, the element–particle conversion algorithm is proposed, which converts the distorted elements into particles based on a given criteria to avoid element distortion. An element is converted into particles when either its equivalent plastic strain or its degree of element distortion exceeds a user-specified value. The degree of element distortion can be evaluated by the ratio of minimum area and the maximum area of the element surfaces taking the hexahedral element as an example. Of course, other criteria could also be used.

For the sake of clarity, take the quadrilateral element as an example to show the conversion algorithm in detail. Fig. 3 shows a quadrilateral finite element mesh with a boundary defined by FE nodes a, b,..., and n. Elements A and B are designated as candidates for conversion to particles. It is common that four particles are placed uniformly in a cell in MPM in 2D problems. Therefore, elements *A* and *B* are removed from the finite elements list and replaced by four particles, respectively.

In order to guarantee the mass momentum and energy conservation, the mass, volume, and internal energy of the element A and B are averaged to the four particles equally. The stress, strain and other history variables of the four particles are set to those of the Gauss points of replaced element. As shown in Fig. 4, the positions of the particles are calculated via the shape function with a specified nature coordinates $(\pm 0.5, \pm 0.5)$ by

$$x_{ip} = \sum_{I=1}^{4} N_I(\pm 0.5, \pm 0.5) x_{iI} \tag{25}$$

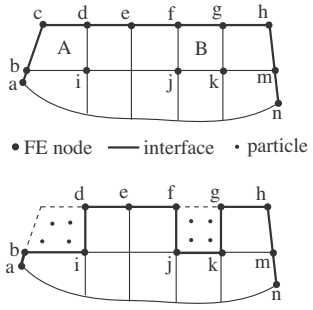

Fig. 3. Conversion of finite elements to particles.

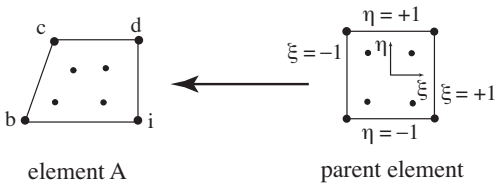

Fig. 4. Calculation of particles position.

where x_{iI} is the position of the FE node *I*. Then, the velocities of the particles are set as those of the adjacent FE nodes. Place background grid to cover all the particles.

The FE node c which is not connected to any elements is removed from the FE nodes list, while the FE nodes b, i, d, f, j, k, and g located at the interface between MPM particles and remaining finite elements are labeled as transition nodes whose nodal mass are reduced by the removal of elements.

After conversion, one Gauss point quadrature is replaced by four particles quadrature with the conservation of mass momentum and energy, and the finite element mesh is replaced by background grid. In 3D problems, one hexahedral element is replaced by eight MPM particles in a similar way.

4. Coupling between finite elements and MPM particles

The coupling between the remaining finite elements and MPM particles is implemented by the transition nodes based on the background grid in MPM framework. The momentum equations of particles in MPM are solved on the background grid and the incremental strain of particles are calculated from the velocity field of the background grid, which imply that the interaction and connection between particles are carried out via the background grid. Therefore, the momentum equations of transition nodes are solved on the background grid together with the particles to establish the interaction and connection between FEM domain and MPM domain.

For the sake of clarity, take a 2D problem shown in Fig. 5 as an example. The material domain is discretized by finite elements in its left part and by MPM particles in the remaining part. The FE nodes a, b and c located at the interface between FEM domain and MPM domain are termed as transition nodes. In each time step, the mass, momentum and nodal force of transition nodes are mapped to the background grid nodes abreast with MPM particles. Taking the grid node *I* shown in Fig. 6 as an example, the nodal mass of grid node *I* is given by

$$m_I = \sum_{p=1}^{n_p} N_{Ip} m_p + \sum_{t=1}^{n_t} N_{It} m_t \tag{26}$$

where the subscript t denotes the transition node, n_t is the total number of transition nodes. The nodal momentum of grid node *I* is obtained by

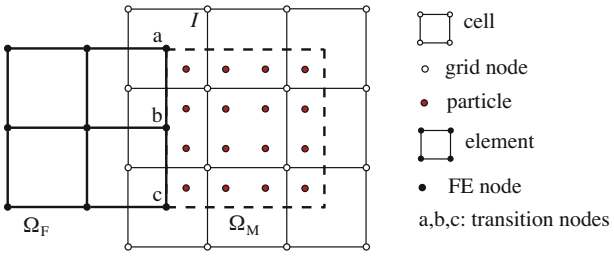

Fig. 5. Coupling between FEM and MPM.

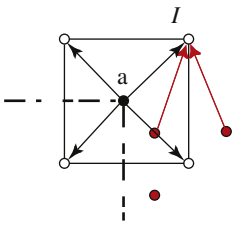

Fig. 6. Grid node *I*.

$$p_{il} = \sum_{p=1}^{n_p} N_{lp} p_{ip} + \sum_{t=1}^{n_t} N_{lt} p_{it} \tag{27}$$

and the external nodal force of grid node I is obtained by

$$f_{il}^{\text{ext}} = \sum_{p=1}^{n_p} m_p N_{lp} b_{ip} + \sum_{t=1}^{n_t} N_{lt} f_{it} \tag{28}$$

where f_{it} is the nodal force of transition node without the hourglass-resisting force.

The velocity field used for the calculation of incremental strain of elements and particles must be identical. Hence, the velocity of the transition nodes must be reset by mapping the velocities of grid nodes back to the transition nodes before calculating the element strain by

$$v_{it} = \sum_{l=1}^{n_g} N_{tl} v_{il} \tag{29}$$

After solving the momentum equations on background grid, the velocities and positions of transition nodes are updated, respectively, by

$$v_{it}^{k+1/2} = v_{it}^{k-1/2} + \Delta t^k \sum_{l=1}^{n_g} f_{il}^k N_{pI}^k / m_I^k + f_{it}^{\Gamma,k} / m_t \Delta t^k \tag{30}$$

$$x_{it}^{k+1} = x_{it}^k + \Delta t^{k+1/2} \left(\sum_{l=1}^{n_g} p_{il}^{k+1/2} N_{pI}^k / m_I^k + f_{it}^{\Gamma,k} / m_t \Delta t^k \right) \tag{31}$$

where $f_{it}^{\Gamma,k}$ is the hourglass-resisting force. Therefore, the velocity field and displacement field are consistent along the interface between FEM domain and MPM domain.

In AFEMP method, a contact/friction/separation algorithm is implemented based on the background grid to handle the contact event between different bodies. The basic idea is to map the information of particles and FE nodes located at the surface of the bodies to the background grid which is used to search for the contact interface and calculate the contact forces between different bodies to prevent the penetration. The detail of the contact method is presented in [35] and will not be repeated here.

5. Implementation of the method

The detailed implementation of AFEMP method in a time step can be summarized as follows.

1. Redefine the background grid, map the mass momentum of all MPM particles and transition nodes to the background grid by Eqs. (26) and (27), respectively.
2. Reset the velocity of the transition nodes by the velocity field of the background grid by Eq. (29).
3. Update the stress. In AFEMP, the stress is updated at the MPM particles and element centers. The Jaumann stress rate is used in the stress update. The strain rate and the spin tensor are calculated by

$$\dot{\varepsilon}_{ijp}^{k-1/2} = \frac{1}{2} \sum_{I=1}^{8} \left[N_{Ip,j}^k v_{iI}^{k-1/2} + N_{Ip,i}^k v_{jI}^{k-1/2} \right] \tag{32}$$

$$\Omega_{ijp}^{k-1/2} = \frac{1}{2} \sum_{I=1}^{8} \left[N_{Ip,j}^k v_{iI}^{k-1/2} - N_{Ip,i}^k v_{jI}^{k-1/2} \right] \tag{33}$$

where the subscript p denotes the particle in MPM region and denotes the Gauss point in finite element region.

4. Calculate the FEM nodal force by

$$f_{ie}^k = f_{ie}^{k,\text{int}} + f_{ie}^{k,\text{ext}} + f_{ie}^{k,\Gamma} \tag{34}$$

and the MPM grid nodal force by

$$f_{il}^k = \sum_{p=1}^{n_p} m_p N_{Ip}^k b_{ip}^k - \sum_{p=1}^{n_p} N_{Ip,j}^k \sigma_{ijp} \frac{m_p}{\rho_p} + \sum_{t=1}^{n_t} N_{It}^k f_{it}^k \tag{35}$$

5. Solve the momentum equations at the background grid nodes in MPM region, and at FE nodes except for the transition nodes in FEM region.
6. Update the velocity and position of FE nodes by Eqs. (21) and (22), MPM particles by Eqs. (23) and (24), and transition nodes by Eqs. (30) and (31), respectively.
7. Loop over all the FE nodes located at the surface of the FEM domain, and convert any distorted elements connected with these nodes into MPM particles based on the conversion scheme presented in Section 3. Label the nodes located at the updated interface between FEM domain and MPM domain as transition nodes, and delete the converted elements and the FE nodes which are not connected to any elements.
8. Discard the deformed background grid for MPM.

The implementation of the contact method is not given here, which has been described in detail in [35].

6. Numerical examples

6.1. Symmetric rods impact

The impact of two symmetric elastic rods shown in Fig. 7 is first studied to validate the accuracy of the coupling scheme in AFEMP. Two rods with length of $l_0 = 21$ mm are traveling at an equal and opposite velocity of $v_0 = 100$ m/s towards each other.

In order to study this problem with 3D codes, the sectional area of the rods is chosen as 3 mm × 3 mm. The density, elastic modulus and Poisson's ratio of the rods are chosen as $\rho = 2.75$ g/cm^3, $E = 65$ GPa and $\nu = 0$, respectively. Symmetric boundary conditions are applied along the four sides parallel to the x axis in both rods. Hence, the analytical separation time and stress distribution can be obtained based on the 1D wave propagation theory. The analytical peak stress during the contact of both rods is $\sigma = -v_0\sqrt{E\rho} = -1336.97$ MPa, and the analytical separation time of the contact process is $t = 2l_0/\sqrt{E/\rho} = 8.63$ μs.

Both the element size and cell size are chosen as 0.5 mm. To assess the effect of particle density on the accuracy of MPM results, this problem is studied using MPM in which the rods are discretized initially by 1, 8 and 27 particles/cell (p/c), respectively. The

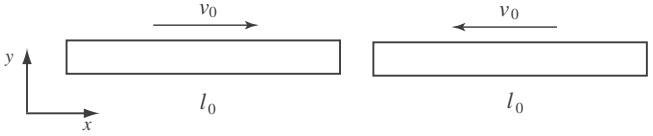

Fig. 7. Symmetric rods impact schematic.

stress profiles along the rods at impact time 2.8 μs obtained by FEM and MPM with various particle densities are compared in Fig. 8(a). It shows that for small deformation problems, MPM with 1 p/c initial discretization gives the worst results, while FEM gives the best results. It also shows that the more particles used initially in a cell, the better results obtained. However, the MPM solutions suffer significant oscillation in stresses in all cases due to the cell crossings noise of particles [21]. In order to eliminate cell crossing noise of particles, Bardenhagen and Kober proposed a GIMP method [21], which is evaluated by Wallstedt and Guilkey [36]. Recently, Zhang et al. proposed a dual domain material point method by modifying the gradient of the shape function for smoother result [37]. Here, this problem is also solved by GIMP algorithm with different particle densities, and the results are shown in Fig. 8(b). There is no significant oscillation in stresses in 1 and 8 p/c cases, whose results are much better than that of MPM. However, the results of GIMP with 27 p/c show significant oscillation in stresses due to that the GIMP weighting functions tend toward those of MPM as more particles are used [21]. As Bardenhagen suggested, fewer particles/cell used is advantageous for GIMP. Generally speaking, the FEM results are more accurate than those of both MPM and GIMP for small deformation problems, and the best choice for p/c value is 8 for MPM with the computational effort taken into account.

To investigate the convergence of MPM, GIMP and FEM, the normalized error in stresses $\bar{e}_{L_2} = ||e||_{L_2}/||\sigma^{ex}(x)||_{L_2}$ is studied, where

$$||e||_{L_2} = ||\sigma^{ex}(x) - \sigma^{h}(x)|| = \left(\int_{x_1}^{x_2} (\sigma^{ex}(x) - \sigma^{h}(x))^2 dx\right)^{1/2}$$

is the Lebesque (L_2) norm, $x_1 = -21$ mm, $x_2 = 21$ mm. By using the nodal integration, the normalized error can be rewritten as $\bar{e}_{L_2} = \sqrt{\sum_I (\sigma_e - \sigma_I)^2/N}/\sigma$, where σ_I is the value of the stress on grid node I distributed along x direction of rod, σ_e is the corresponding analytical solution which takes the value of either 0 or σ, σ is the analytical peak stress in the rod, and N is the total number of gird nodes in x direction whose analytical stress equals σ. Take the stress profiles value at time 2.8 μs as a sample, Fig. 9 compares the normalized errors of FEM solution with those of MPM and GIMP solutions for different particles densities. It is shown that the accuracy and convergence rate of FEM are higher than that of both MPM and GIMP in this small deformation problem, and the accuracy of 8 p/c case is higher than others in GIMP results. The convergence rate of all the methods is lower than 1 for this dynamic problem.

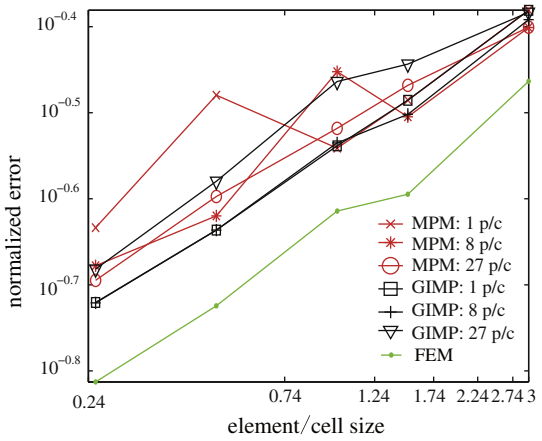

Fig. 9. The normalized error for MPM, GIMP and FEM.

In AFEMP, cell crossing noise of particles occurs only in the MPM domain, which can be reduced by using GIMP. The difference between GIMP and MPM is mainly due to the shape functions, so GIMP can be implemented in AFEMP as similar to MPM. This problem is studied again using AFEMP with GIMP. As shown in Fig. 10, one part of each rod with length of 9 mm is modeled by GIMP, and the rest part by FEM. Each rod is discretized by 864 hexahedral elements with element size 0.5 mm together with 5184 particles with space of 0.25 mm. There is no element–particle conversion for this small deformation problem and the cell size of the background grid is taken as 0.5 mm, so the particle density is 8 p/c.

The separation time of the contact process obtained by the AFEMP is 8.7 μs, which is close to the analytical result 8.63 μs. Besides, the stress profiles obtained by both AFEMP and GIMP are also in good agreement with analytical result as shown in Fig. 11 which shows that wave reflection exists at the interface between FEM and

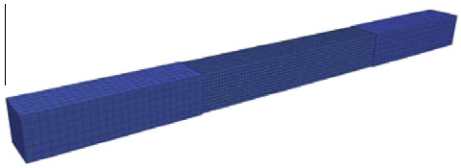

Fig. 10. Discretization model of AFEMP with GIMP.

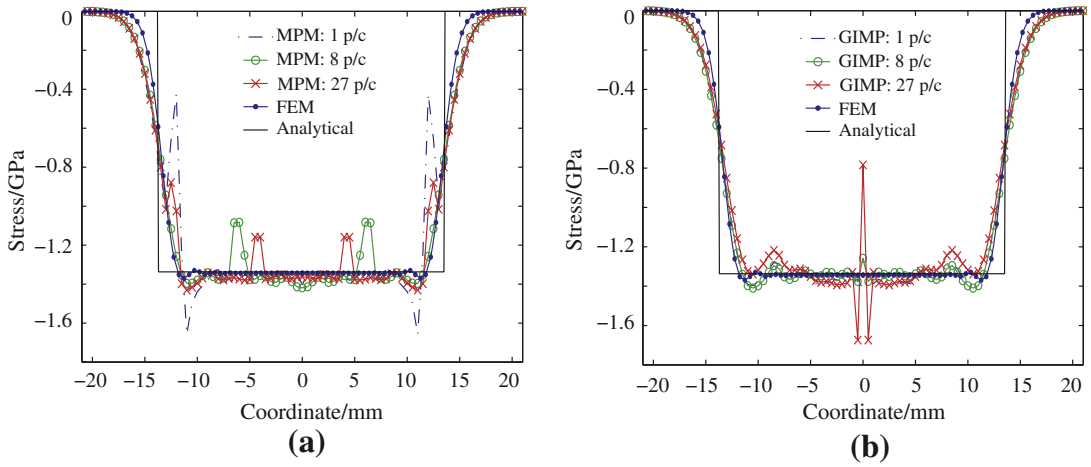

Fig. 8. Numerical and analytical results of the symmetric rods impact at time 2.8 μs: (a) MPM and FEM, (b) GIMP and FEM.

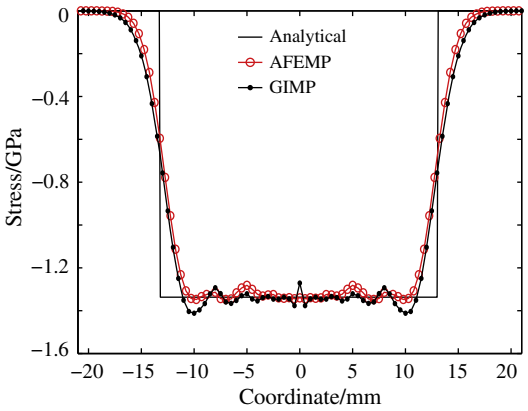

Fig. 11. Stress profiles at time 2.7 μs.

GIMP domain due to the different discretization types, but it has little effect on the final results. Furthermore, the energy curves obtained by AFEMP is plotted in Fig. 12 which shows good energy conservation.

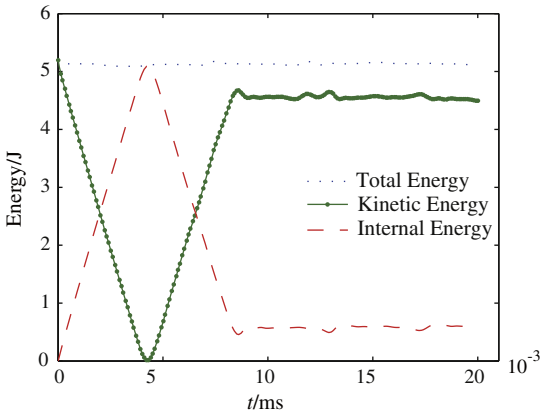

Fig. 12. Energy evolution.

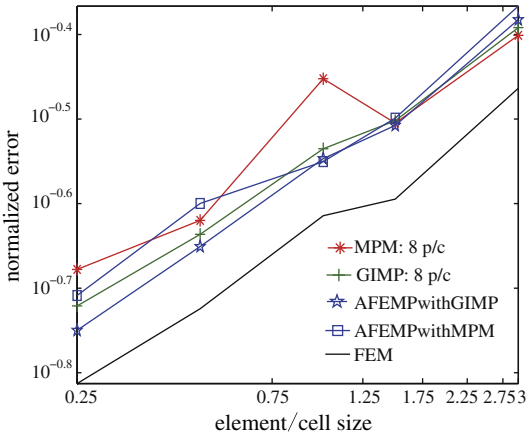

Fig. 13. The normalized error for MPM, GIMP, FEM and AFEMP.

Table 1
Material constants of the cylinder.

ρ (g/mm^3)	E (MPa)	v	A (MPa)	B (MPa)	n	C
8.93×10^{-3}	117×10^3	0.35	157	425	1.0	0.0

To further investigate the performance of AFEMP, the convergence rate for AFEMP with GIMP and AFEMP with MPM is studied and plotted in Fig. 13, which shows that the convergence rate of AFEMP with GIMP is between that of FEM and GIMP and close to GIMP, while the convergence rate of AFEMP with MPM is between that of FEM and MPM and close to MPM.

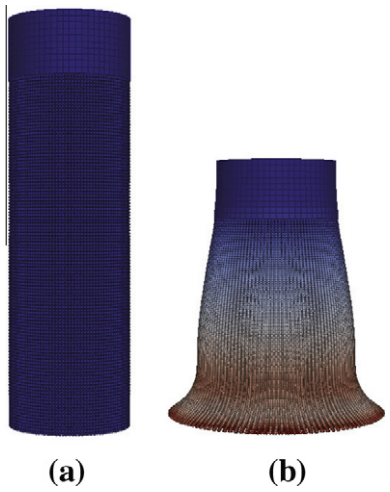

Fig. 14. (a) Discretization model and (b) the final shape of the cylinder.

Table 2
The final length and diameter of the deformed bar.

	L (mm)	D (mm)
Experiment	16.2	13.5
AFEMP	16.21	13.2
MPM	16.21	13.2

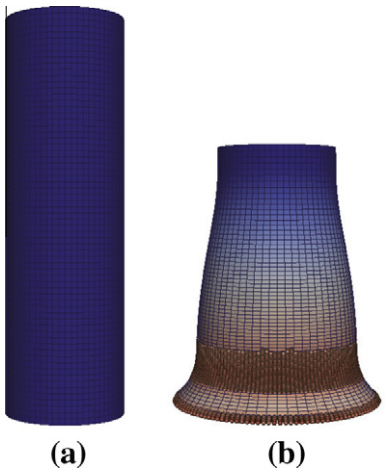

Fig. 15. (a) Discretization model and (b) the final shape of the cylinder.

Table 3
The final length and diameter of the deformed bar obtained with different threshold.

	Threshold	L (mm)	D (mm)
Experiment		16.2	13.5
AFEMP	0.7	16.33	13.28
AFEMP	0.8	16.32	13.34
AFEMP	0.9	16.32	13.35
AFEMP/FEM	∞	16.31	13.36

Table 4
Computational cost.

	Δt_{max} (μs)	Δt_{min} (μs)	Steps	CPU (s)
FEM	1.27×10^{-2}	0.60×10^{-2}	10,752	929
MPM	3.46×10^{-2}	3.01×10^{-2}	2423	970
AFEMP (0.7)	1.27×10^{-2}	1.19×10^{-2}	6672	1208
AFEMP (0.9)	1.27×10^{-2}	1.19×10^{-2}	6670	884

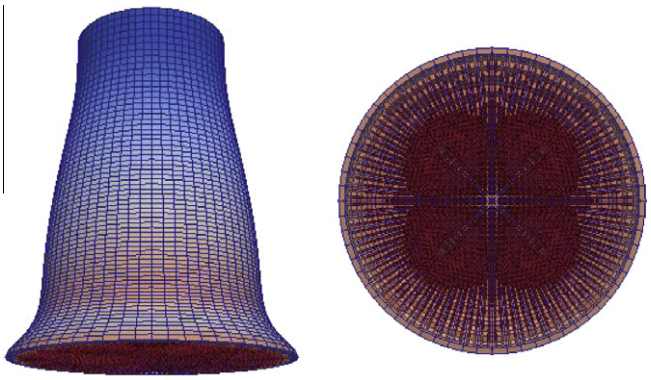

Fig. 16. The final configuration of the bar with threshold 0.9.

Table 5
Material constants in the Johnson–Cook model.

Material	A (GPa)	B (GPa)	n	C	m	T_{ref} (K)	T_{melt} (K)
Steel	0.75	1.15	0.49	0.014	1	293	1700
Tungsten	1.05	0.177	0.12	0.0275	1	293	1723

Table 6
Material constants in the Gruneisen EOS.

Material	c (m/s)	s	γ
Steel	3570	1.92	1.8
Tungsten	4030	1.24	1.8

Although the results of GIMP are smoother than those of MPM, GIMP requires much more computational cost than MPM, especially in 3D problems. Hence, MPM is used in AFEMP for the following examples with the particle density of 8 p/c.

6.2. Taylor bar impact

The second example is the typical Taylor bar test conducted by Johnson and Holmquist [38]. A cylinder with an initial velocity of 190 m/s travels to a rigid wall. The initial length and diameter of the cylinder are $l_0 = 25.4$ mm and $D_0 = 7.6$ mm, respectively. Johnson–Cook model is applied for the cylinder with the material constant listed in Table 1.

The discretization model is shown in Fig. 14(a). The top part with length of 3.8 mm is discretized by 7680 hexahedral elements and 8811 FE nodes, while the bottom part by 144,324 MPM particles with cell size 0.36 mm and particle space about 0.19 mm. The final length and diameter of the deformed bar obtained by AFEMP and MPM are compared with the experimental data in Table 2. The final configuration of the cylinder is shown in Fig. 14(b).

6.3. Taylor bar impact with conversion

The previous problem is studied again with the conversion scheme. All the geometry sizes and material constants are the same to those used in the previous problem. The bar is initially discretized by 51,456 hexahedral elements as shown in Fig. 15(a), where the maximum element size is 0.38 mm. When the equivalent plastic strain of an element exceeds the given threshold, it is converted into eight particles with the background cell size of 0.38 mm. To study the effect of the threshold on the result, different thresholds are used as listed in Table 3. If there is no conversion, AFEMP yields the same results as the FEM.

Table 3 compares the final length and diameter of the deformed bar obtained by the AFEMP with the experimental data. The final configuration of the cylinder with the threshold of 0.7 is shown in Fig. 15(b). Furthermore, the computational cost required by MPM and AFEMP with different threshold is compared in Table 4. For AFEMP without conversion, namely FEM, the minimum time step, Δt_{min}, is about one half of the maximum time step, Δt_{max}, due to no extreme deformation occurred, so its efficiency is higher than MPM. For AFEMP with conversion threshold 0.7, the minimum time step is larger than that of FEM due to the conversion, but its computational cost is higher than those of both FEM and MPM because the total number of time steps is greater than that of MPM and many elements are converted into particles. However, the computational cost of AFEMP with threshold 0.9 is lower than those of both FEM and MPM due to that less elements are converted into particles as shown in Fig. 16 and the total time steps is less than that of FEM. So, this example shows that FEM is more efficient than MPM for problems without element distortion. Besides, AFEMP may be less efficiency than both FEM and MPM due to inappropriate threshold applied, but is more efficient than both FEM and MPM with a appropriate threshold.

Table 7
Results of simulation and experiment.

Case	Result of	Residual length ratio	Residual velocity ratio
I	Experiment	0.85	0.97
	AFEMP	0.82	0.96
	MPM	0.85	0.96
II	Experiment	0.76	0.99
	AFEMP	0.72	0.97
	MPM	0.74	0.97

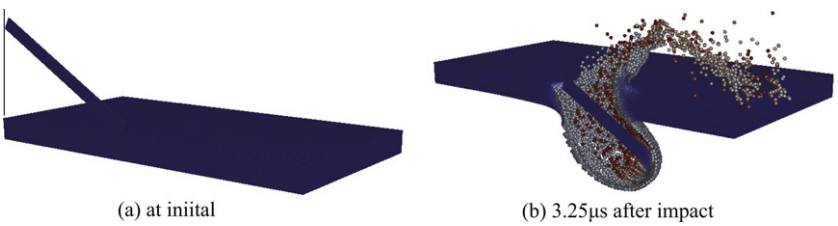

Fig. 17. The discretization model for WHA projectile and plate target.

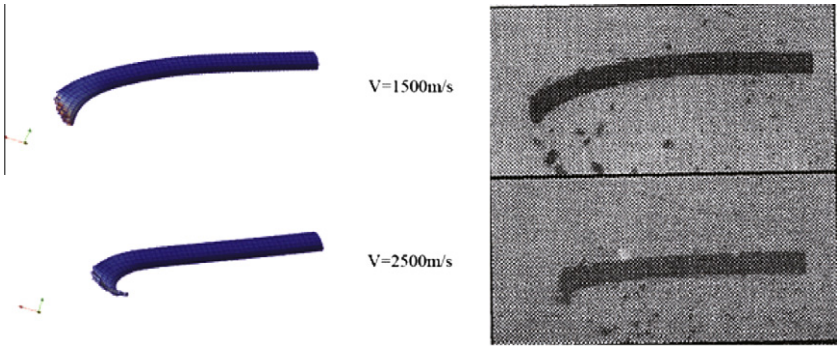

Fig. 18. Residual part of projectile.

6.4. Projectile penetration

The WHA long rod projectile penetration experiment [39] is studied. The projectiles hit steel armor plates under an angle of 60° at different initial velocities. The length and the diameter of the projectile are 75 and 5 mm, respectively, while the size of the target is 150 mm × 150 mm with different thickness. Two cases are studied. In the first case, the initial velocity of the projectile is 1500 m/s and the thickness of the target is 5 mm; in the second case, the initial velocity is 2500 m/s, and the thickness is 9 mm.

The Johnson–Cook model and Gruneisen equation of state are used for both projectile and target, and the material constant taken from [39–41] are listed in Tables 5 and 6, respectively. An effective plastic strain failure model with threshold of 0.9 is used for both projectile and target [41].

Due to the symmetry, half of the model is studied as shown in Fig. 17(a). Symmetrical boundary condition is applied in the symmetry surface, while free boundary condition is applied elsewhere. The regular hexahedral element with element size of 1 mm is used for the target. The total number of elements for the target is 56,250 in the first case and 101,250 in the second case. For both cases, 1824 hexahedral elements are used for the projectile model. One element is converted into eight MPM particles when its effective plastic strain exceeds 0.9 during the simulation process as shown in Fig. 17(b) for the second case.

The projectile's residual length ratios and residual velocity ratios obtained by AFEMP and experiment are compared in Table 7, which shows that numerical results obtained by AFEMP agree well with experimental data. The residual part of the projectile obtained by AFEMP is also in good agreement with the experimental data as shown in Fig. 18 for both cases.

Besides, the two cases are studied by MPM again. In order to fix the numerical accuracy of MPM and AFEMP for the objective comparison of computational efficiency, the cell size and particle space of MPM discretization are also set to 1 and 0.5 mm, respectively. The numerical results of MPM are listed in Table 7, which is close to AFEMP results. The computational cost required by AFEMP and MPM for the second case are compared in Table 8, which shows that AFEMP is much more efficient than MPM in this impact simulation, although the total number of time steps used by AFEMP almost double that used by MPM.

6.5. Soil collapse

The final numerical example is a 2D soil collapse experiment conducted by Bui et al. [42], in which many small aluminum bars of diameters 1.0 and 1.5 mm were used to model soil. These bars were initially arranged into a rectangular area 200 mm× 100 mm, which is generated by standing two flat solid walls on a flat surface as shown in Fig. 19. The experiment was started by quickly removing the right wall horizontally to one side. Then the aluminum bars will flow down to the side due to the gravity, and the final state of the aluminum bars is shown in Fig. 21.

Table 8
Computational cost required by MPM and AFEMP.

	Δt_{max} (μs)	Δt_{min} (μs)	Steps	CPU (s)
MPM	6.45×10^{-2}	3.71×10^{-2}	1180	2241
AFEMP	3.67×10^{-2}	1.52×10^{-2}	2208	838

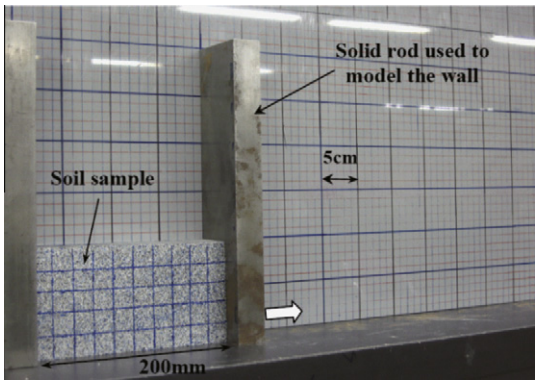

Fig. 19. Arrangement of soil collapse experiment.

Table 9
Material constants in Drucker–Prager model.

ρ (g/mm^3)	K (MPa)	c	ϕ	ψ
2.65×10^{-3}	0.7	0	19.8	0

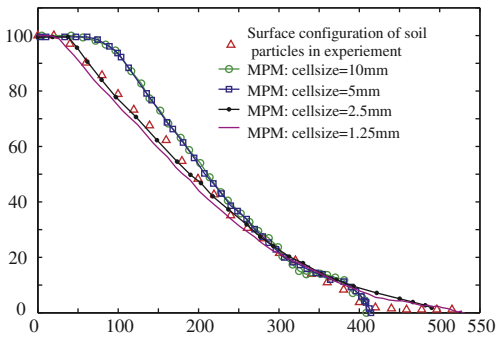

Fig. 20. Final surface configurations obtained by MPM with various cell sizes.

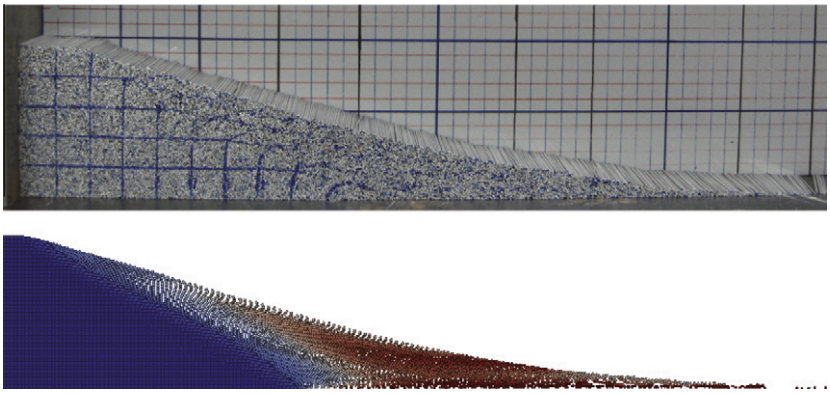

Fig. 21. Final shape of soil.

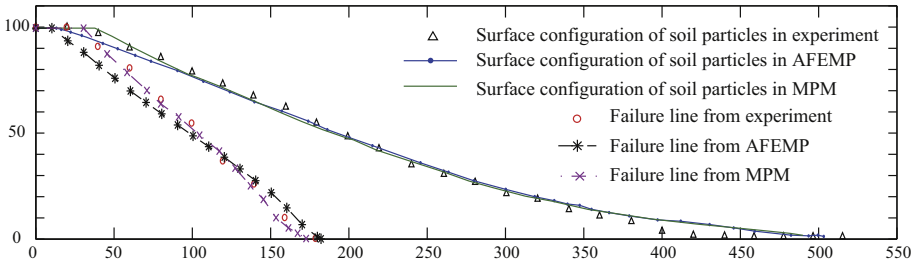

Fig. 22. Final surface configurations and failure lines.

Table 10
Computational cost required by MPM and AFEMP.

	Δt_{max} (μs)	Δt_{min} (μs)	Steps	CPU (s)
MPM	48.41	29.94	34,765	1791
AFEMP	48.41	22.85	47,402	1123

Drucker–Prager constitutive is used for the soil, and the material constant is taken from [42] as listed in Table 9. In order to study this problem by 3D code, the plain strain assumption is used for the following discretization models.

Considering that the Drucker–Prager constitutive is a local model, a mesh convergence is studied to investigate the cell size effect in MPM. Four cases are simulated with cell size of 10, 5, 2.5, and 1.25 mm, respectively. In each case, the particle space is one half of the cell size which means there are eight particles in each cell. The both side surfaces and the left side of the discretization model are set as symmetrical boundaries. The bottom surface is set as fixed boundary according to the settings given in [42], while others are set as free boundaries. The surface configurations obtained by MPM are compared with experimental data in Fig. 20, which shows that the cases with cell size of 2.5 and 1.25 mm are close to each other and agree well with experimental curve. That is to say cell size of 2.5 mm is a good choice for this problem.

Then this example is simulated by AFEMP with the element size of 2.5 mm to fix the numerical accuracy with MPM. Hence, 3200 hexahedral elements are initially used in the discretization model, and one element is converted into eight particles when its effective plastic strain exceeds 1.2 during the simulation process. The boundary conditions are similar to MPM settings. The final shape of the soil obtained by AFEMP is compared with the final shape of aluminum bars obtained by the experiment in Fig. 21, while the surface configurations and failure lines obtained by AFEMP and MPM are compared with experimental results in Fig. 22, which shows that two numerical results are close to each other and agree well with experimental data. Furthermore, the computational cost required by AFEMP and MPM are listed in Table 10 which also shows that AFEMP is more efficient than MPM.

7. Conclusion

In this paper, an adaptive finite element material point (AFEMP) method is presented, which uses FEM for the material domain during the mild deformation stage and MPM for the same material domain during the extreme deformation stage. The conversion of distorted finite elements to MPM particles is adaptive based on a user specified criteria. The coupling between finite elements and MPM particles is implemented by solving the momentum equations of FE transition nodes, located at the interface between finite elements domain and MPM particles domain, together with particles on the background grid. Therefore, AFEMP method takes full the efficiency of FEM for mild deformation and capacity of MPM for extreme deformation. Due to the same shape functions used in both FEM and MPM, the wave reflection from the interface is little. Numerical results have been presented to demonstrate the capability of AFEMP method. For mild deformation problems, AFEMP method without element–particle conversion is identical with FEM. For extreme deformation problems, AFEMP method is more efficient than both FEM and MPM, while the numerical results are in good agreement with analytical results and experiment data.

References

[1] S. Cen, X.M. Chen, C.F. Li, X.R. Fu, Quadrilateral membrane elements with analytical element stiffness matrices formulated by the new quadrilateral area coordinate method (qacm-ii), Int. J. Numer. Meth. Eng. 77 (8) (2009) 1911–1944.
[2] S. Cen, M.J. Zhou, X.R. Fu, A 4-node hybrid stress-function (hs-f) plane element with drilling degrees of freedom less sensitive to severe mesh distortions, Comput. Struct. 89 (2011) 517–528.

[3] W.K. Liu, T. Belytschko, H. Chang, An arbitrary lagrangian-eulerian finite element method for path-dependent materials, Comput. Methods Appl. Mech. Eng. 58 (1986) 227–245.
[4] J.J. Monaghan, An introduction to sph, Comput. Phys. Commun. 48 (1988) 89–96.
[5] M.B. Liu, G.R. Liu, Z. Zong, K.Y. Lam, Computer simulation of high explosive explosion using smoothed particle hydrodynamics methodology, Comput. Fluids 32 (3) (2003) 305–322.
[6] T. Belytschko, Y.Y. Lu, L. Gu, Element free galerkin methods, Int. J. Numer. Meth. Eng. 372 (1994) 229–256.
[7] X.F. Pan, H. Yuan, Computational algorithm and application of element-free galerkin methods for nonlocal damage models, Eng. Fract. Mech. 77 (2010) 2640–2653.
[8] W.K. Liu, S. Jun, Y.F. Zhang, Reproducing kernel particle methods, Int. J. Numer. Meth. Fluids 20 (1995) 1081–1106.
[9] J.S. Chen, C. Pan, C.T. Wu, et al., Reproducing kernel particle methods for large deformation analysis of nonlinear structures, Comput. Meth. Appl. Mech. Eng. 139 (1996) 195–227.
[10] S.R. Idelsohn, E. Onate, N. Calvo, et al., The meshless finite element method, Int. J. Numer. Meth. Eng. 58 (6) (2003) 893–912.
[11] G.R. Johnson, Linking of Lagrangian particle methods to standard finite element methods for high velocity impact computations, Nucl. Eng. Des. 150 (1994) 265–274.
[12] T. Belytschko, D. Organ, Y. Krongauz, A coupled finite element-element-free galerkin method, Comput. Mech. 17 (1995) 186–195.
[13] T.D. Vuyst, R. Vignjevic, J.C. Campbell, Coupling between meshless and finite element methods, Int. J. Impact Eng. 31 (2005) 1054–1064.
[14] W.K. Liu, R.A. Uras, Y. Chen, Enrichment of the finite element method with reproducing kernel particle method, J. Appl. Mech. 135 (1997) 143–166.
[15] G.R. Johnson, R.A. Stryk, S.R. Beissel, et al., An algorithm to automatically convert distorted finite elements into meshless particles during dynamic deformation, Int. J. Impact Eng. 27 (10) (2002) 997–1013.
[16] G.R. Johnson, R.A. Stryk, Conversion of 3d distorted element method for hypervelocity impact simulation, Int. J. Impact Eng. 28 (2003) 947–966.
[17] T. Rabczuk, S.P. Xiao, M. Sauer, Coupling of mesh-free methods with finite elements: basic conceptes and test results, Commun. Numer. Meth. Eng. 22 (2006) 1031–1065.
[18] E.P. Fahrenthold, B.A. Horban, A hybrid particle-finite element method for hypervelocity impact simulation, Int. J. Impact Eng. 23 (1999) 237–248.
[19] D. Sulsky, Z. Chen, H.L. Schreyer, A particle method for history-dependent materials, Comput. Meth. Appl. Mech. Eng. 118 (1–2) (1994) 179–196.
[20] S. Ma, X. Zhang, X.M. Qiu, Comparison study of mpm and sph in modeling hypervelocity impact problems, Int. J. Impact Eng. 36 (2009) 272–282.
[21] S.G. Bardenhagen, E.M. Kober, The generalized interpolation material point method, Comput. Model. Eng. Sci. 5 (6) (2004) 477–495.
[22] S. Ma, X. Zhang, Y.P. Lian, X. Zhou, Simulation of high explosive explosion using adaptive material point method, Comput. Model. Eng. Sci. 39 (2) (2009) 101–123.
[23] S.G. Bardenhagen, J.U. Brackbill, D. Sulsky, The material-point method for granular materials, Comput. Meth. Appl. Mech. Eng. 187 (3–4) (2000) 529–541.
[24] S.G. Bardenhagen, J.E. Guilkey, K.M. Roessig, et al., An improved contact algorithm for the material point method and application to stress propagation in granular material, Comput. Model. Eng. Sci. 2 (4) (2001) 509–522.
[25] P. Huang, X. Zhang, S. Ma, X. Huang, Contact algorithms for the material point method in impact and penetration simulation, Int. J. Numer. Meth. Eng. 85 (4) (2011) 498–517.
[26] Z.T. Ma, X. Zhang, P. Huang, An object-oriented MPM framework for simulation of large deformation and contact of numerous grains, Comput. Model. Eng. Sci. 55 (2010) 61–87.
[27] W. Hu, Z. Chen, A multi-mesh mpm for simulating the meshing process of spur gears, Comput. Struct. 81 (2003) 1991–2002.
[28] W. Hu, Z. Chen, Model-based simulation of the synergistic effects of blast and fragmentation on a concrete wall using the MPM, Int. J. Impact Eng. 32 (12) (2006) 2066–2096.
[29] Y.P. Lian, X. Zhang, X. Zhou, et al., Numerical simulation of explosively driven metal by material point method, Int. J. Impact Eng. 38 (2011) 237–245.
[30] H.W. Zhang, K.P. Wang, Z. Chen, Material point method for dynamic analysis of saturated porous media under external contact/impact of solid bodies, Comput. Meth. Appl. Mech. Eng. 198 (2009) 1456–1472.
[31] S. Andersen, L. Andersen, Modelling of landslides with the material-point method, Comput. Geosci. 14 (2010) 137–147.
[32] J.A. Nairn, Material point method calculations with explicit cracks, Comput. Model Eng. Sci. 4 (2003) 649–663.
[33] D.Z. Zhang, Q. Zou, W.B. VanderHeyden, X. Ma, Material point method applied to multiphase flows, J. Comput. Phys. 227 (2008) 3159–3173.
[34] X. Zhang, K.Y. Sze, S. Ma, An explicit material point finite element method for hyper-velocity impact, Int. J. Numer. Meth. Eng. 66 (4) (2006) 689–706.
[35] Y.P. Lian, X. Zhang, Y. Liu, Coupling of finite element method with material point method by local multi-mesh contact method, Comput. Meth. Appl. Mech. Eng. 200 (2011) 3482–3494.
[36] P.C. Wallstedt, J.E. Guilkey, An evaluation of explicit time integration schemes for use with the generalized interpolation material point method, J. Comput. Phys. 227 (2008) 9628–9642.
[37] D.Z. Zhang, X. Ma, P.T. Giguere, Material point method enhanced by modified gradient of shape function, J. Comput. Phys. 230 (2011) 6379–6398.
[38] G.R. Johnson, T.J. Holmquist, Evaluation of cylinder-impact test data for constitutive model constants, J. Appl. Phys. 64 (8) (1988) 3901–3910.
[39] L. Holmberg, P. Lundberg, L. Westerling, An experimental investigation of wha long rods penetrating oblique steel plates, in: 14th International Symposium on Ballistics, 1993.
[40] E. Liden, J. Ottosson, L. Holmberg, Wha long rods penetrating stationary and moving oblique steel plates, in: 16th International Symposium on Ballistics, 1996.
[41] Y.K. Park, E.P. Fahrenthold, A kernel free particle-finite element method for hypervelocity impact simulation, Int. J. Numer. Meth. Eng. 63 (2005) 737–759.
[42] H.H. Bui, R. Fukagawa, K. Sako, S. Ohno, Lagrangian meshfree particles method (sph) for large deformation and failure flows of geomaterials using elastic-plastic soil constitutive model, Int. J. Numer. Anal. Meth. Geomech. 32 (2008) 1537–1570.